2023 IEEE International Conference on Robotics and Automation (ICRA 2023)
May 29 - June 2, 2023. London, UK

Modular Multi-axis Elastic Actuator with Torque Sensing Capable p-CFH for Highly Impact Resistive Robot Leg

Youngrae Kim, Sunghyun Choi, Jinhyeok Song, and Dongwon Yun*, *Senior Member, IEEE*

***Abstract*— This study proposes a modular Multi-axis Elastic Actuator (MAEA) for legged robots that can effectively cope with impacts that may occur during dynamic maneuvering. MAEA has multi-axis compliance and can measure the torque without additional encoders. Therefore, effective impact resistance is possible with less volume and weight than conventional Series Elastic Actuators (SEA). The 6-axis stiffness analysis of paired-Crossed Flexural Hinge (p-CFH) is extended from small deformation to large deformation, and the accuracy is verified through Finite Element Analysis (FEA) and experiments. Based on the analysis, the torque of p-CFH is measured, and feedback torque control is also performed. Finally, the robot leg was constructed with MAEA, and the multi-axis impact resistance performance of MAEA was demonstrated by analyzing the applied impact during landing experiments at various angles.**

I. Introduction

With the flow of technological development, modern robots are breaking down the boundaries of their application range. Robots are not limited to the precise position control performance required by traditional industrial robots but are required to have the ability to surpass animals, such as by enabling physical interactions and dynamic motions. This view presents several challenges in terms of robot design and control. In the case of a legged robot, it is essential to design a suitable robot actuator to withstand the ground reaction force, overcome various types of terrain and obstacles, and perform dynamic motions such as running, jumping, and backflipping at high speed. Therefore, it is necessary to design actuators to generate high output power and withstand possible impacts or disturbances in the environment.

Geared motors used in legged robots [1] have high force control performance and can carry a large load through a high gear ratio and torque sensor, however, such motors have high rigidity, low backdrivability, and heavy and expensive sensors. It is not easy to adapt these motors to high impact situations, so they are not suitable for dynamic movements. Accordingly, the Quasi-Direct Drive (QDD), which consists of a high torque density motor and a low gear ratio, has appeared [2], [3]. With its high backdrivability, this actuator can engage in high-speed driving, jumping, and backflips [4]. However, the diameter of the high torque density motor is large, and the output torque is low due to the low gear ratio, and so QDD is used for small loads. In addition, there is a Series Elastic Actuator (SEA) that can endure impacts via the attachment of an elastic element between the motor and the load [5], [6]. SEA consists of a high gear ratio motor, a spring, and an additional encoder for torque measurement; closed-loop force control is thus possible [7]. By decoupling the actuator from the impact through a spring, excellent impact resistance is achieved, and actuators are used in StarlETH [8], ANYmal [9], [10]. In addition, there are cases in which variable stiffness elements are used in robots, rather than fixed stiffness [11]. However, additional springs and encoders increase weight and volume and have a low torque control bandwidth. Also, the spring of modular SEA has only single-axis compliance because it is constrained to motor rotation [9], [12], [13].

This work was supported by the National Research Foundation of Korea (NRF) grant funded by the Korea government (MSIT) (No. 2020R1C1C1012279). *(* Corresponding author: Dongwon Yun.)*

Authors are with the Department of Robotics and Mechatronics Engineering, Daegu Gyeongbuk Institute of Science and Technology (DGIST), Daegu, 42988 South Korea (e-mail: wutzahaha@dgist.ac.kr; csh7369@dgist.ac.kr; songjinhuk@dgist.ac.kr; mech@dgist.ac.kr).

Fig. 1: paired-Crossed Flexural Hinge with rotating.

When the foot of a robot leg interacts with the environment, the impact occurs not only in the rotational direction but is applied in an arbitrary direction in space. Therefore, this paper developed a modular Multi-axis Elastic Actuator (MAEA) that can mitigate multi-axis impacts. The paired-Crossed Flexural Hinge (p-CFH) structure with 6-axis compliance [14] was applied to MAEA. Stiffness analysis of p-CFH was conducted, and a strategy was presented to measure the displacement and torque of p-CFH without an additional encoder. Finally, MAEA was found to have excellent impact resistance and torque sensing with smaller volume and weight than SEA. Feedback torque control was achieved through the manufactured MAEA, and multi-axis impact resistance performance was evaluated by landing experiments performed on MAEA robot leg.

II. Elastic Mechanism for Actuator

The elastic mechanism design of an elastic actuator is an essential factor influencing the overall actuator performance. There are cases in which torsional springs are used [12], and fabricated flexure mechanisms are used [15] for elastic mechanisms. These methods limit the adaptation to the environment because the spring's displacement is constrained by translational or rotational motion. Unlike these mechanisms, the p-CFH structure (Fig. 1), which is also used in robot joints [14], [16], has excellent impact resistance due to its 6-axis

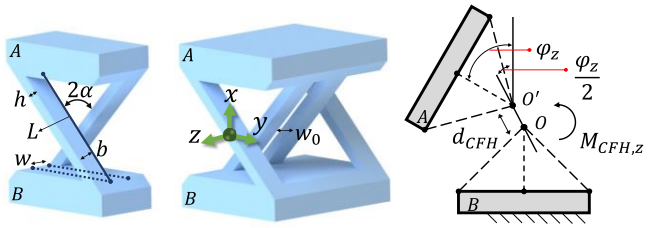

(a) (b) (c)

Fig. 2: (a) Crossed Flexural Hinge. (b) paired-Crossed Flexural Hinge. (c) Rotated shape of CFH.

compliance. Also, there is no backlash and friction, no need for lubrication, and it can be designed to have the desired stiffness.

A. p-CFH Stiffness Analysis

Crossed Flexural Hinges (CFH) have structures in which two leaf springs of length L, width b, and thickness h intersect at an angle of 2α with an interval w to connect upper and lower links A and B, as shown in Fig. 2a. p-CFH is illustrated in Fig. 2b, in which CFH faces symmetrically with an interval of w_0. 6-axis stiffness analysis of CFH was performed under small deformation conditions by Bellouard [17]. Yang et al. [14] extended stiffness analysis to p-CFH; the z-axis rotational stiffness doubled, and y-axis rotational stiffness increased by about 20 times compared to those of CFH. However, due to the relatively low z-axis rotational stiffness, p-CFH rotates with a large nonlinear deformation along the z-axis, so the rotational displacement cannot be expressed for the fixed point O. Therefore, the rotational displacement φ_z was redefined, as shown in Fig. 2c, considering the center shift d_{CFH} that occurs during large deformation. Ultimately, we seek to obtain z-axis nonlinear rotational stiffness for φ_z.

Several methods exist to interpret the large deformation behavior of leaf springs [18], [19]. Methods to extend from this concept to analyze the large deformation behavior of CFH include the Elastica Theory (EL) method [20] and the Pseudo Rigid Body Model (PRBM) [21], [22]. It has been validated that the analysis result of the EL method shows a minor error with Finite Element Analysis (FEA) [23]. The EL method derives solutions of the Euler-Bernoulli beam equation through elliptical integration, and the relationship between the moment $M_{CFH,z}$ and the rotational displacement φ_z, as shown in Fig. 2c, can be obtained. Since this process involves elliptical integration and the solving of numerical solutions, the computational load is large, making this method difficult to apply to robots in real-time. However, approximation is possible because $M_{CFH,z}$ is represented as third-order polynomial for φ_z [20]. When E is Young's modulus, ν is Poisson's ratio, and I is the smallest linear moment of inertia of the spring ($I = bh^3/12$), the relationship can be approximated by a polynomial form of $M_{CFH,z}\,L/2EI\varphi_z = K_M(\alpha)\varphi_z^2 + 1$. The coefficient K_M can be expressed using a second-order polynomial for α, as follows.

$$K_M = 0.833\alpha^2 - 0.6841\alpha + 0.1855 \qquad (1)$$

$$M_{CFH,z} = \frac{2EI}{L}(K_M\varphi_z^3 + \varphi_z) \qquad (2)$$

Values of coefficients were fitted with a coefficient of determination higher than 0.9995 in the range of $\pi/6 < \alpha < 5\pi/18$ (low buckling & large rotation range), $-\pi/6 < \varphi_z < \pi/6$ (low yield). Finally, $M_{p-CFH,z}$ was derived using the following equation.

$$M_{p-CFH,z} = 2M_{CFH,z} = \frac{4EI}{L}(K_M\varphi_z^3 + \varphi_z) \qquad (3)$$

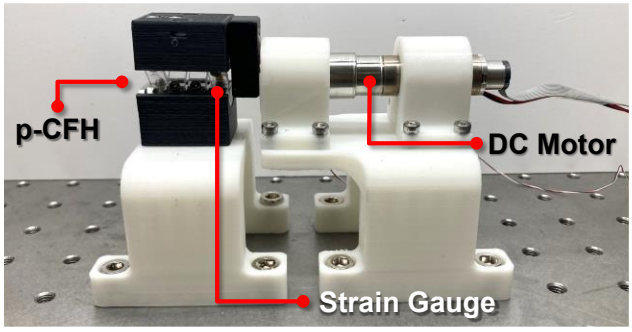

(a)

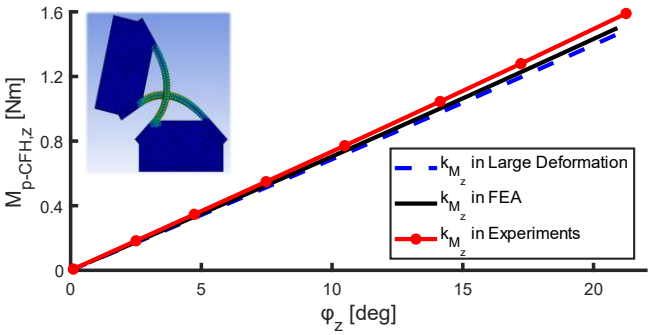

(b)

Fig. 3: (a) Moment experimental setup. (b) Comparison of nonlinear stiffness for large deformation analysis with FEA and experiment results.

To confirm the accuracy of the large deformation stiffness analysis, results were compared with FEA and experimental results. FEA analysis was executed through the Ansys program (Ansys Mechanical, Ansys, USA), and the experiment was performed through a moment experiment device, as shown in Fig 3a. The springs made of Polycarbonate (PC) material were used to achieve excellent resiliency of p-CFH; the property values of the utilized p-CFH were as follows: $\alpha = \pi/4, L = 10\ mm, b = 6\ mm, h = 2\ mm, w = 1\ mm, w_0 = 1\ mm, E = 2.45\ Gpa, \nu = 0.36$. The Young's modulus of the material was measured using a universal testing machine (KUM-5A, KM&T, Korea). Moment was applied to p-CFH through torque control using a DC motor and controller (Geared Encoder DC Motor & EPOS2 24/2 DCX Controller, Maxon, Switzerland), and the rotational displacement was measured through Tracker, an open-source video analysis program, to calculate the final rotational stiffness. Finally, comparison results are as shown in the graph in Fig. 3b. When $\varphi_z = 20°$, the relative error between the experiment result and the FEA was 4.3%, indicating that the experiment was accurately performed. The nonlinear stiffness, obtained through the large deformation analysis, showed relative errors of 2.5% and 6.5% with FEA and experimental results at $\varphi_z = 20°$; analysis result accuracy was also verified.

Applying the large deformation analysis result to the 6-axis stiffness matrix of p-CFH [14] leads to the following equations.

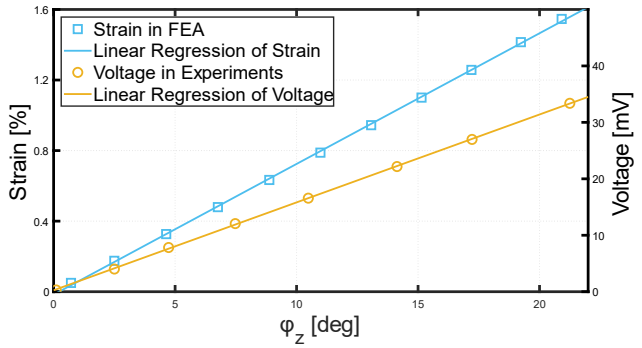

(a)

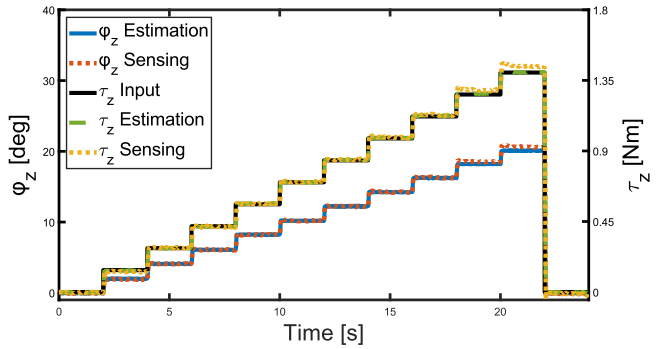

(b)

Fig. 4: (a) Linearity of between rotational displacement and strain & voltage. (b) Torque sensing performances compared with torque input and estimation.

$$\begin{bmatrix} F_x \\ F_y \\ F_z \\ M_x \\ M_y \\ M_z \end{bmatrix} = \begin{bmatrix} k_{F_x} & 0 & 0 & 0 & 0 & 0 \\ 0 & k_{F_y} & 0 & 0 & 0 & 0 \\ 0 & 0 & k_{F_z} & 0 & 0 & 0 \\ 0 & 0 & 0 & k_{M_x} & 0 & 0 \\ 0 & 0 & 0 & 0 & k_{M_y} & 0 \\ 0 & 0 & 0 & 0 & 0 & k_{M_z} \end{bmatrix} \begin{bmatrix} x \\ y \\ z \\ \theta_x \\ \theta_y \\ \varphi_z \end{bmatrix} \tag{4}$$

$$\begin{bmatrix} k_{F_x} k_{M_x} \\ k_{F_y} k_{M_y} \\ k_{F_z} k_{M_z} \end{bmatrix} = \tag{5}$$

$$2E \begin{bmatrix} \left(\frac{bh}{L} + \frac{bh^2}{L^3}\right)\left(\frac{hb^3}{12L} + \frac{bh^3}{3L(2v+2)} + \frac{bh^3\left\{\left(\frac{3b+w_0}{2}+w\right)^2 + \left(\frac{b+w_0}{2}\right)^2\right\}}{L^3}\right) \\ \left(\frac{bh}{L} + \frac{bh^3}{L^3}\right)\left(\frac{hb^3}{12L} + \frac{bh^3}{3L(2v+2)} + \frac{bh\left\{\left(\frac{3b+w_0}{2}+w\right)^2 + \left(\frac{b+w_0}{2}\right)^2\right\}}{L}\right) \\ 2\left(\frac{hb^3}{L^3}\right) \qquad\qquad \left(\frac{bh^3}{6L}\right)(K_M\varphi_z^3 + \varphi_z) \end{bmatrix}$$

As a result, for real-time analysis of p-CFHs used in robot actuators, a 6-axis stiffness analysis method with improved accuracy was derived by extending small deformation analysis to large deformation through approximation using EL method.

B. p-CFH Sensing

In this research, the actuator volume, weight, and price were reduced by directly measuring the deformation of the p-CFH used in the modular actuator through a strain gauge and calculating the torque. First, linearity between the strain and rotational displacement of the spring was validated through FEA and experiments. In FEA, the strain and rotational displacement of the spring were directly derived. In the case of the experiment, the strain cannot be measured directly. However, since the strain gauge outputs a voltage linearly proportional to the strain of the attached material, the output voltage and rotational displacement were measured, and a linear relationship was identified according to the relationship below.

$$\varepsilon \propto V, \quad if\ V \propto \varphi_z, \quad \therefore \varepsilon \propto \varphi_z \tag{6}$$

A strain gauge (MMF402183, Vishay Measurements Group, USA) was attached to the center of one spring of p-CFH using an adhesive for gauges. The p-CFH was installed in the moment experiment device shown in Fig. 3a. A quarter bridge circuit and 16-bit analog-to-digital converter (ADC) were used to measure the output voltage of the gauge, and the Tracker program was used to measure the rotational displacement of p-CFH. As illustrated in Fig. 4a, in both cases, the coefficient of determination of the linear regression within the rotational displacement of 20° was more than 0.9997, so it can be judged to be linear. Second, it was confirmed that the spring strain occurred within the strain range of the strain gauge. The allowable strain range of the utilized strain gauge was $\pm 1.5\%$. According to the FEA data shown in Fig. 4a, in the range of rotational displacement less than 20°, the strain range satisfies the condition of 1.5%, so it can be confidently used.

Through the linearity, it is possible to linearly scale the voltage of the strain gauge to the rotational displacement of the p-CFH. Therefore, the transmitted moment to p-CFH could be calculated through equation (3) with rotational displacement that scaled from output voltage of strain gauge. Since p-CFH has 6-axis compliance, external force/torque can be transmitted not only in pure z-axis moment, but also in other axial directions. However, the axial stiffness except z-axis have relatively large values, so we could assume that p-CFH will deform within a small range and recover quickly. According to the assumption, the transmitted torque is calculated as follows: $\tau_z \cong M_{p-CFH,z}$. The torque measurement performance of p-CFH was evaluated using the moment experiment device. First, a torque is applied to the p-CFH and the measured output voltage values are scaled with a rotational displacements. Then, a constantly increasing torque is applied, and rotational displacement and torque are sensed according to the above description. The torque values measured through the strain gauge are compared with the input torque values and estimated torque values through the current sensing of the motor. The results are shown in Fig. 4b. In the section of $\tau_z < 1.4\ Nm$, the average value of the relative error between the torque estimation and sensing was about 1.34%. It verified that the voltage values can be linearly scaled to the rotational displacement values and equation (3) accurately maps the relationship between rotational displacement and torque. In the section of $\tau_z \geq 1.4\ Nm$, the average relative error between the estimation and the sensing values increases as 2.84% because the torque cannot be applied as a pure z-axis moment as other axes moments were increased. This phenomenon will be solved in the future by measuring and compensating the deformation of other axes by installing additional strain gauges.

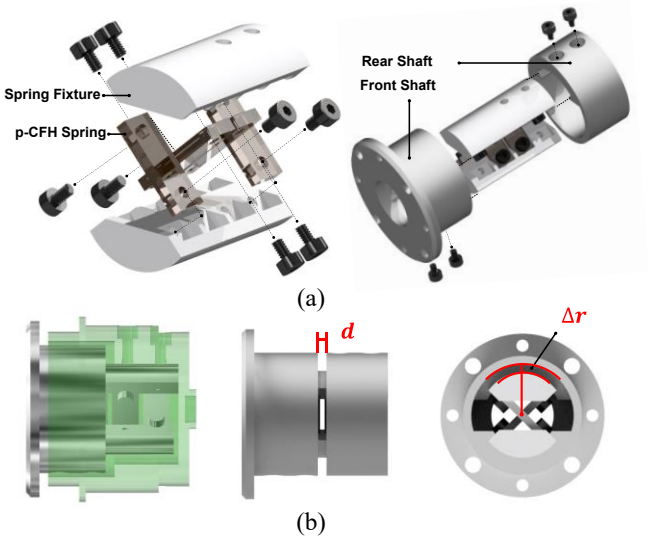

Fig. 5: (a) Assembly process of p-CFH shaft. (b) p-CFH shaft workspace representation.

III. Actuator Design and Control

Legged robots composed of elastic actuators do not exhibit dynamic maneuvers. Although there may be no direct effect, increasing the torque bandwidth and precise control may not be a solution. In the case of Salto [24], [25], a rubber spring was adequately utilized to achieve a jump, and performance was excellent for jumps up to $1.25\,m$. In this way, elastic actuators may overcome their limitations when elastic springs are optimally used. Accordingly, in this paper, we propose a modular MAEA for legged robots, starting with optimizing the spring performance by maximizing the multi-axis impact resistance of the elastic mechanisms.

A. Multi-Axis Elastic Actuator with p-CFH Shaft

For MAEA to absorb external impact, the shaft was constructed through a p-CFH, as shown in Fig. 5. The p-CFH springs are fastened to the upper and lower spring fixtures and are designed to be replaceable, and the upper and lower spring fixtures are fastened to the front and rear shafts. The properties of p-CFH are the same as seen in the previous chapter. The space d between the front and rear shaft and the space Δr between the fixture and shaft define the workspace and stable operating area of p-CFH and stops motion with link contact. The Δr value was set to have a safety factor of approximately 1.4 when $1.4\,Nm$ torque was applied to the z-axis and p-CFH was rotated by $20°$. d value was chosen to have a workspace of about $1\,mm$ and $3°$ for different axial force/torque.

The MAEA design is depicted in Fig. 6a. The p-CFH shaft was assembled with the two bearings and rotor of the motor to transmit power. The bearings and stator were fixed to the motor housing and the driver were fixed to the driver housing. All housings were made of aluminum. The motor uses a frameless inrunner BLDC (RI-70, T-Motor, China) for compact engagement with the designed p-CFH shaft. It has a $0.94\,Nm$ continuous torque, $2.68\,Nm$ peak torque, $8.4\,A$ continuous current, and $24\,A$ peak current. The gear was not considered in the evaluation of only the actuator sensing, torque control, and impact resistance performance. The weight of the hardware was $560\,g$ and the size is $86\,\emptyset \times 51\,mm$, and the finally manufactured MAEA is shown in Fig. 6b.

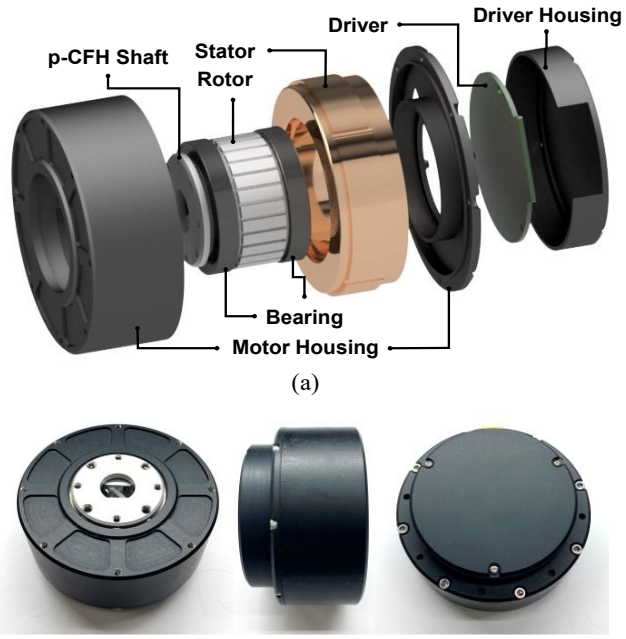

Fig. 6: (a) Expanded view of the actuator. (b) The modular multi-axis elastic actuator with fully assembled.

C. Electronics and Communication

MAEA uses a BLDC controller that used for MIT Mini Cheetah, which is open-source [4]. The controller includes a magnetic position sensor, uses Field Oriented Control (FOC) to control the motor current at a loop rate of $40\,kHz$, receives the position, speed, feedforward torque, and gain value commands, and returns position, speed, and torque values. The controller has allowable $30\,A$ continuous current and $40\,A$ peak current, suitable for the utilized motor. The controller uses $1\,kHz$ CAN Bus communication suitable for legged robots using multiple actuators. The strain gauge attached to the p-CFH returns a measured torque value through the ADC; feedback torque control is also possible. The torque sensing resolution is $0.04\,Nm$ which is acceptable that compared to other legged robots torque sensors [1], [9], and range is $1.4\,Nm$ which can be adjusted by changing the p-CFH properties.

D. Actuator Feedback Control

Based on the previously demonstrated torque sensing of p-CFH, MAEA is capable of feedback torque control. For verification, MAEA was connected to a commercial 6-axis force/torque (F/T) sensor (HEX-E QC, OnRobot, Denmark) as shown in Fig. 7a. Assuming little backlash because of p-CFH and no gear, torque control was performed without backlash compensation according to the linear torque control strategy with the PD controller [26]. The torque tracking performance of MAEA was validated for square and sinusoidal wave torque input, and the feedback torque value was compared with the estimated torque value through the motor current and the torque measurement value of the F/T sensor. The comparison results are shown in the graph of Fig. 7b. For a magnitude of about 30% of $1.4\,Nm$, the actuator tracks the reference torque well in both cases with rising time $0.025\,s$ and 2% steady-state errors on average. Despite the 12.5% motor torque

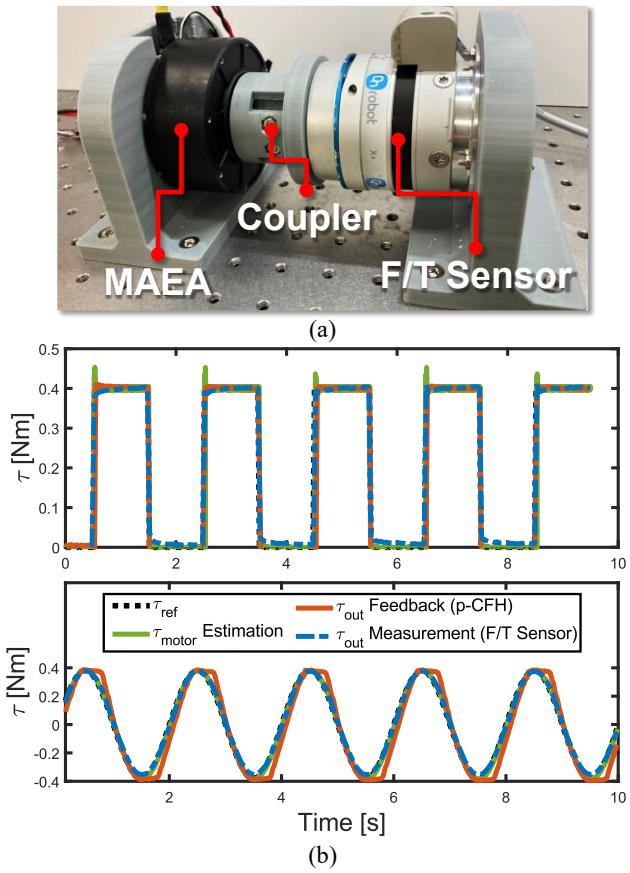

Fig. 7: (a) Feedback torque control experimental setup with actuator and F/T sensor. (b) Tracking performance with MAEA torque feedback and F/T sensor measurements.

overshoot when using square input, the output torque delivered through the spring overshoot is reduced to 4.5% due to the damping characteristic of the spring. As a result, when the feedback torque was compared with the measured value of the F/T sensor, we demonstrated that MAEA was able to control the output torque of the precise magnitude. The closed-loop torque control bandwidth performance was also analyzed through the frequency response of excitation experiments under fixed load conditions, as illustrated in Fig. 8. It can be validated that the closed-loop torque control bandwidth was 45 Hz for the amplitudes that 20% of 1.4 Nm.

A. Multi-axis Impact Resistance

Effective jumping performance was also demonstrated by using impedance control to cope with impact when the legged robot landed its foot on the ground [27]. However, the control may not absorb an impact when the robot is driving due to the attack angle, driving direction, or unknown environmental elements. In this perspective, MAEA has passive multi-axis impact resistance that can protect the robot by isolating the motor part from external force/torque. The impact resistance performance can be maintained through high y-axis rotational stiffness [14] even when constructing a robot leg using multiple MAEAs.

B. Multi-axis Impact Resistance Performances

To evaluate the multi-axis impact resistance performance of MAEA, a 2-degree of freedom (DOF) robot leg with MAEA was manufactured, as illustrated in Fig. 9a. The legs were

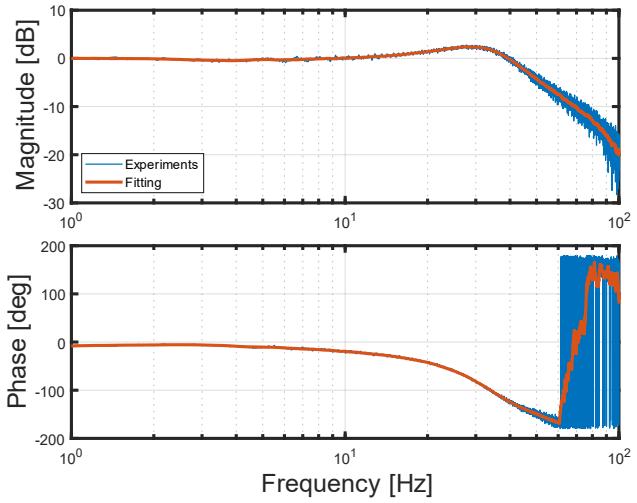

Fig. 8: Frequency response of the MAEA's closed-loop torque control.

fabricated using a 3D printer (M300, Zortrax, Poland). The leg length/actuator weight ratio of MIT Mini Cheetah capable of high dynamic motions is 0.4 m/kg [4], which is a large value compared to other quadrupedal robots [2], [8], [9]. From that, the lengths of the upper and lower links were determined as 0.169 m and 0.164 m. To reduce inertia, both knee and hip actuators were located on the robot body, and the lower link was connected to the knee actuator through a Poly Chain belt. A 6-axis F/T sensor was attached to the hip actuator and robot leg was attached to a linear guide to measure the force/torque from impact during landing sequences. The total system weight was about 1.7 kg including legs, actuators, and sensor. As shown in Fig. 9a, the angle between the ground and the linear guide that leg attached is defined as the landing angle. The landing angle was set at 90°, 60°, and 30°, and the robot's forward speed increased as the landing angle decreased. This is an indirection application of increasing the attack angle of legs to increase the forward speed when the quadrupedal robot is actually moving. The initial height of the foot was set to 0.15 m from the ground in all cases.

For evaluation of the MAEA multi-axis impact resistance performance, force/torque measurements upon landing were compared when the Motor, single-axis SEA, and MAEA were used for the leg. The Motor was constructed by replacing the p-CFH shaft with a simple cylindrical shape shaft, and the single-axis SEA was implemented by filling the space ($d = 0$) in Fig 5 with low friction material and constraining compliance except for rotation. In all cases, the actuator performed position control to maintain its virtual link length at 0.20 m. The experimental results can be seen in the graph in Fig. 9b. In all landing angle cases, impact due to a fall and 1st contact occurred. When landing angle was 90°, a 2nd contact from a slight jump occurred due to the large ground reaction force. Maximum impact occurred during the 1st contact period. F_x, F_y, F_z and τ_x, τ_y, τ_z values were compared for each actuator cases. For 90° and 60° cases, impact was mainly composed of F_y, otherwise, on the other way, F_x is the main component on 30° case. τ_x mainly composed the impact in all landing angle cases. All force/torque values show trend of Motor > SEA > MAEA in every landing angles. For more efficient comparison at each actuator cases, the magnitude of

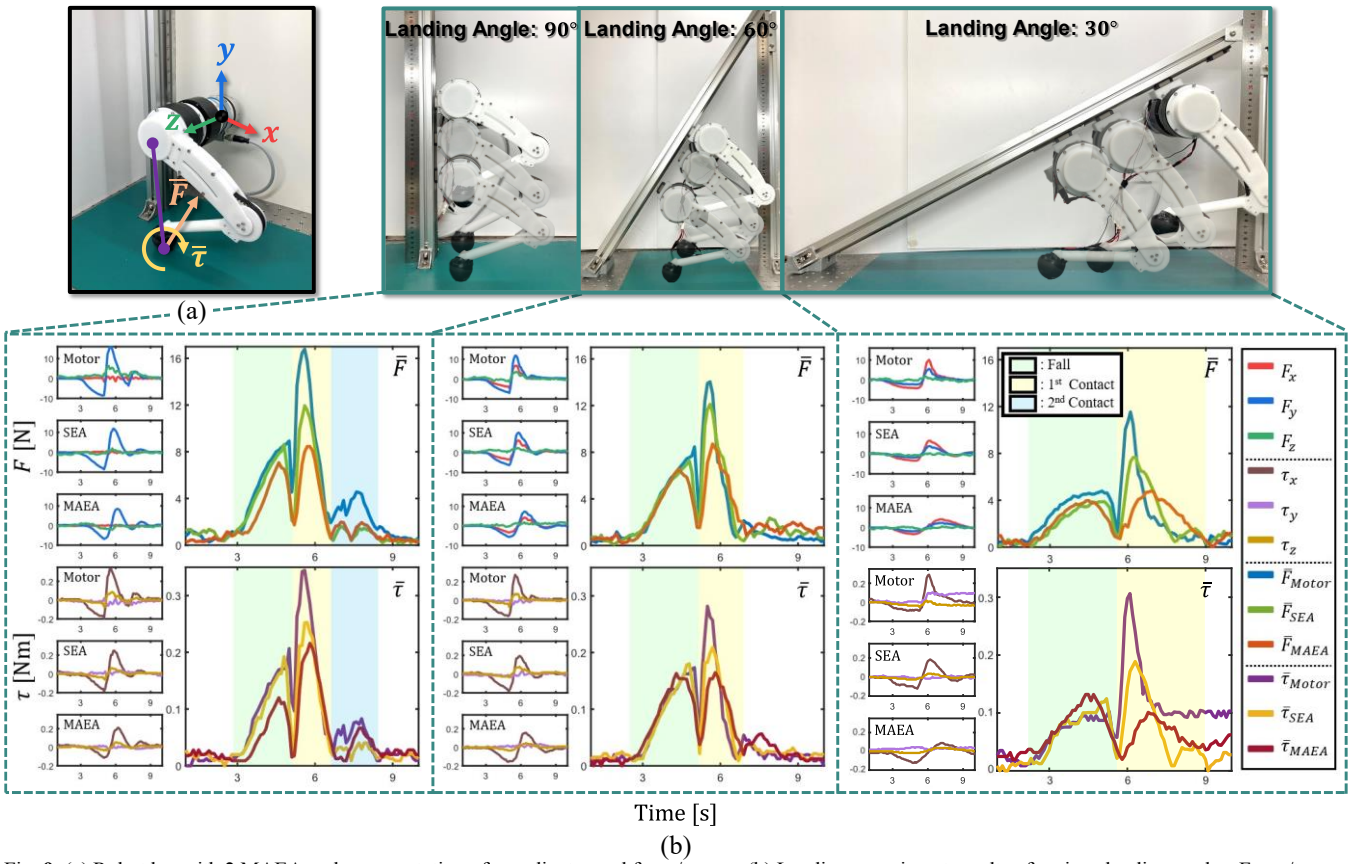

Fig. **9**: (a) Robot leg with 2 MAEA and representation of coordinates and force/torque. (b) Landing experiment results of various landing angles. Force/torque and their vector sum of Motor, SEA, and MAEA are compared.

the force/torque vector sum $\bar{F}$ and $\bar{\tau}$ of each actuator were derived. In the impact size comparison, the vector sum shows the same trend as before. At the 1st contact in 90° case, the maximum $\bar{F}_{MAEA}$ was decreased by about 8.3 N and 3.5 N compared to maximum $\bar{F}_{Motor}$ and $\bar{F}_{SEA}$. And maximum $\bar{\tau}_{MAEA}$ was decreased by about 0.1 Nm and 0.04 Nm compared to maximum $\bar{\tau}_{Motor}$ and $\bar{\tau}_{SEA}$. In addition, $\bar{F}_{MAEA}$ became about 50.3% and 70.7% of $\bar{F}_{Motor}$ and $\bar{F}_{SEA}$, and $\bar{\tau}_{MAEA}$ became about 61.7% and 84% of $\bar{\tau}_{Motor}$ and $\bar{\tau}_{SEA}$ on average for 90° case. Also, $\bar{F}_{MAEA}$, $\bar{\tau}_{MAEA}$ became 62%, 72% and 57%, 80% in 60°, and $\bar{F}_{MAEA}$, $\bar{\tau}_{MAEA}$ became 41 %, 62 % and 43%, 72% in 30 ° of $\bar{F}_{Motor}, \bar{F}_{SEA}$ and $\bar{\tau}_{Motor}$, $\bar{\tau}_{SEA}$. Therefore, it could be sorted MAEA leg transmitted 41% less impact than the Motor and 33% less impact than the SEA on average. In other words, it was validated through landing experiments at various angles that the MAEA robot leg effectively separated the impact from the robot through multi-axis impact resistance. However, looking at the $\bar{F}$ and $\bar{\tau}$ values after landing, the vibration magnitude of MAEA was larger than SEA due to its multi-axis compliance. Because of these characteristics, it is essential to design the stiffness of the MAEA's p-CFH according to the robot specification. Proposed MAEA shows that vibration converged within 1 second and soon became the same as Motor and SEA case. As a result of experiments, we can see the possibility that when a legged robot is configured with MAEA, it will be able to better cope with various impacts during high-speed dynamic driving.

IV. Conclusion

In this paper, we developed MAEA, which can mitigate impacts more effectively than the existing modular actuators for legged robots. A p-CFH having 6-axis compliance was applied as an elastic mechanism for impact resistance of the actuator. Traditional small deformation stiffness analysis of p-CFH was extended to large deformation; the accuracy was confirmed by the relative errors of 2.5% and 6.5% of the FEA and experiment results. By confirming the torque sensing performance using the strain gauge without an additional encoder, it was verified that torque measurements have a relative error of about 0.23% with the torque estimation value in $\tau_z < 1.4\,Nm$. Feedback torque control was executed through the manufactured MAEA, including the proposed p-CFH shaft structure, and it was confirmed that the torque tracking was well performed through the F/T sensor. Finally, a 2-DOF robot leg was constructed using MAEA, and landing experiments at various angles were conducted. For the cases of using the Motor, SEA, and MAEA, the force/torque values from impact during landing were analyzed it was found that the multi-axis impact resistance transmitted 49% less impact than the Motor and 30% less impact than the SEA on average. So far, no gear has been added to the actuator to evaluate MAEA torque sensing, control, and multi-axis impact resistance performance. In the future, when configuring the entire legged robot system with MAEA, a gear will be added with an appropriate gear ratio and type, considering the specifications of the entire robot.

REFERENCES

[1] Y. H. Lee, Y. H. Lee, H. Lee, H. Kang, J. H. Lee, L. T. Phan, S. Jin, Y. B. Kim, D.-Y. Seok, S. Y. Lee, et al., "Development of a quadruped robot system with torque-controllable modular actuator unit," *IEEE Transactions on Industrial Electronics*, vol. 68, no. 8, pp. 7263–7273, 2020.

[2] P. M. Wensing, A. Wang, S. Seok, D. Otten, J. Lang, and S. Kim, "Proprioceptive actuator design in the mit cheetah: Impact mitigation and high-bandwidth physical interaction for dynamic legged robots," *IEEE transactions on robotics*, vol. 33, no. 3, pp. 509–522, 2017.

[3] S. Yu, T.-H. Huang, X. Yang, C. Jiao, J. Yang, Y. Chen, J. Yi, and H. Su, "Quasi-direct drive actuation for a lightweight hip exoskeleton with high backdrivability and high bandwidth," *IEEE/ASME Transactions on Mechatronics*, vol. 25, no. 4, pp. 1794–1802, 2020.

[4] B. Katz, J. Di Carlo, and S. Kim, "Mini cheetah: A platform for pushing the limits of dynamic quadruped control," in *2019 International conference on robotics and automation (ICRA)*. IEEE, 2019, pp. 6295–6301.

[5] G. A. Pratt and M. M. Williamson, "Series elastic actuators," in *Proceedings 1995 IEEE/RSJ International Conference on Intelligent Robots and Systems. Human Robot Interaction and Cooperative Robots*, vol. 1. IEEE, 1995, pp. 399–406.

[6] K. Kong, J. Bae, and M. Tomizuka, "Control of rotary series elastic actuator for ideal force-mode actuation in human–robot interaction applications," *IEEE/ASME transactions on mechatronics*, vol. 14, no. 1, pp. 105–118, 2009.

[7] S. Oh and K. Kong, "High-precision robust force control of a series elastic actuator," *IEEE/ASME Transactions on mechatronics*, vol. 22, no. 1, pp. 71–80, 2016.

[8] M. Hutter, C. Gehring, M. A. Ho¨pflinger, M. Blo¨sch, and R. Siegwart, "Toward combining speed, efficiency, versatility, and robustness in an autonomous quadruped," *IEEE Transactions on Robotics*, vol. 30, no. 6, pp. 1427– 1440, 2014.

[9] M. Hutter, C. Gehring, D. Jud, A. Lauber, C. D. Bellicoso, V. Tsounis, J. Hwangbo, K. Bodie, P. Fankhauser, M. Bloesch, et al., "Anymal-a highly mobile and dynamic quadrupedal robot," in *2016 IEEE/RSJ international conference on intelligent robots and systems (IROS)*. IEEE, 2016, pp. 38–44.

[10] P. Fankhauser and M. Hutter, "Anymal: a unique quadruped robot conquering harsh environments," *Research Features*, no. 126, pp. 54–57, 2018.

[11] Zhong, Y., Du, R., Guo, P., & Yu, H, "Investigation on a new approach for designing articulated soft robots with discrete variable stiffness," *IEEE/ASME Transactions on Mechatronics*, 26(6), 2998-3009, 2021.

[12] C. Lee and S. Oh, "Development, analysis, and control of series elastic actuator-driven robot leg," *Frontiers in neurorobotics*, vol. 13, p. 17, 2019.

[13] F. Guenther, H. Q. Vu, and F. Iida, "Improving legged robot hopping by using coupling-based series elastic actuation," *IEEE/ASME Transactions on Mechatronics*, vol. 24, no. 2, pp. 413–423, 2019.

[14] J. Yang, J. Kim, D. Kim, and D. Yun, "Shock resistive flexure-based anthropomorphic hand with enhanced payload," *Soft Robotics*, vol. 9, no. 2, pp. 266–279, 2022.

[15] J. P. Cummings, D. Ruiken, E. L. Wilkinson, M. W. Lanighan, R. A. Grupen, and F. C. Sup, "A compact, modular series elastic actuator," *Journal of Mechanisms and Robotics*, vol. 8, no. 4, 2016.

[16] G. Bai and N. Rojas, "Self-adaptive monolithic anthropomorphic finger with teeth-guided compliant cross-four-bar joints for underactuated hands," in *2018 IEEE-RAS 18th International Conference on Humanoid Robots (Humanoids)*. IEEE, 2018, pp. 145-152.

[17] Y. Bellouard, "Microrobotics," *Methods and applications*, CRCPress, Boca Raton, 2010.

[18] K. Bisshopp and D. Drucker, "Large deflection of cantilever beams," *Quarterly of applied mathematics*, vol. 3, no. 3, pp. 272–275, 1945.

[19] L. L. Howell and A. Midha, "Parametric deflection approximations for end-loaded, large-deflection beams in compliant mechanisms," in *International Design Engineering Technical Conferences and Computers and Information in Engineering Conference*, vol. 9402. American Society of Mechanical Engineers, 1992, pp. 157–166.

[20] J. Haringx, "The cross-spring pivot as a constructional element," *Flow, Turbulence and Combustion*, vol. 1, no. 1, pp. 313–332, 1949.

[21] B. D. Jensen and L. L. Howell, "The modeling of cross-axis flexural pivots," *Mechanism and machine theory*, vol. 37, no. 5, pp. 461–476, 2002.

[22] X. Pei, J. Yu, G. Zong, and S. Bi, "An effective pseudo-rigid-body method for beam-based compliant mechanisms," *Precision Engineering*, vol. 34, no. 3, pp. 634–639, 2010.

[23] K. Markovic´ and S. Zelenika, "Optimized cross-spring pivot configurations with minimized parasitic shifts and stiffness variations investigated via nonlinear fea," *Mechanics Based Design of Structures and Machines*, vol. 45, no. 3, pp. 380–394, 2017.

[24] J. K. Yim and R. S. Fearing, "Precision jumping limits from flight-phase control in salto-1p," in *2018 IEEE/RSJ international conference on intelligent robots and systems (IROS)*. IEEE, 2018, pp. 2229-2236.

[25] J. K. Yim, B. R. P. Singh, E. K. Wang, R. Featherstone, and R. S. Fearing, "Precision robotic leaping and landing using stance-phase balance," *IEEE Robotics and Automation Letters*, vol. 5, no. 2, pp. 3422–3429, 2020.

[26] W. Choi, J. Won, J. Lee, J. Park., "Low stiffness design and hysteresis compensation torque control of SEA for active exercise rehabilitation robots," Autonomous robots, vol. 41, no. 5, pp. 1221-1242, 2017.

[27] F. Grimminger, A. Meduri, M. Khadiv, J. Viereck, M. Wu¨thrich, M. Naveau, V. Berenz, S. Heim, F. Widmaier, T. Flayols, et al., "An open torque-controlled modular robot architecture for legged locomotion research," *IEEE Robotics and Automation Letters*, vol. 5, no. 2, pp. 3650–3657, 2020.